Development of a mercuric iodide detector array for medical imaging applications

Bradley E. Patt[a,*], Jan S. Iwanczyk[a], Martin P. Tornai[b], Craig S. Levin[b], Edward J. Hoffman[b]

[a]*Xsirius, Inc., 1220 Avenida Acaso, Camarillo, CA 93012, USA*
[b]*Crump Institute for Biological Imaging, UCLA School of Medicine, 10833 Le Conte Ave., Los Angeles, CA 90024, USA*

Abstract

A nineteen element mercuric iodide (HgI_2) detector array has been developed as a prototype for a larger (169 element) array, which is intended for use as an intra-operative gamma camera (IOGC). This work is motivated by the need for identifying and removing residual tumor cells after the removal of bulk tumor, while sparing normal tissue. Prior to surgery, a tumor seeking radiopharmaceutical is injected into the patient, and the IOGC is used to locate and map out the radioactivity. The IOGC can be used with commercially available radioisotopes such as ^{201}Tl, ^{99m}Tc, and ^{123}I which have low energy X- and gamma-rays. The use of HgI_2 detector arrays in this application facilitates construction of an imaging head that is very compact and has a high signal-to-noise ratio. The prototype detectors were configured as discrete pixel elements joined by fine wires into novel pseudo crossed-grid arrays to promote improved electric field distribution compared with previous designs, and to maximize the fill factor for the expected circular probe shape. Pixel dimensions are hexagonal with 1.5 mm and 1.9 mm diameters separated by 0.2 mm thick lead septa. The overall detectors are hexagonal with a diameter of ~1 cm. The sensitive detector thickness is 1.2 mm, which corresponds to >99% efficiency at 59 keV and 67% efficiency at 140 keV. Row, column, and pixel spectra have been measured on the prototypical detector array. Energy resolution was found to vary with the width of the row/column coincidence window that was applied. With the low edge of the coincidence window at 30% below the photopeak, pixel energy resolutions of 2.98% and 3.88% FWHM were obtained on the best individual pixels at 59 keV (^{241}Am) and 140 keV (^{99m}Tc), respectively. To characterize this array as an imaging device, the spatial response of the pixels was measured with stepped point sources. The spatial response corresponded well with the pixel geometry, indicating that the spatial resolution was determined by the pixel geometry.

1. Introduction

Semiconductor detector array based imaging systems, in particular the compound high Z semiconductor types such as room temperature mercuric iodide (HgI_2) and $Cd_{1-x}Zn_xTe$ (CdZnTe and CdTe) are ideally suited to the development of a new class of small area medical imaging systems. When optimized for particular diagnostic applications these systems offer advantages over scintillation detector systems, predominantly NaI(Tl) scintillators coupled to photomultiplier tubes (PMTs). Advantages include superior energy resolution, pixel array features with spatial resolution defined by the electrode patterning, and

room temperature operation. Furthermore, smaller area devices facilitate close detector-to-object separation, which improves both sensitivity and spatial resolution in emission imaging.

Our work has focused on the development of a small area HgI_2 detector array with the design optimized for intra-operative surgical procedures. The device would be used with a tumor seeking radiopharmaceutical with a high tumor to normal tissue affinity, e.g. ^{99m}Tc-sestamibi or labeled monoclonal antibody injected prior to surgery. After the removal of the bulk tumor, such as in neurosurgery, the surgeon localizes the residual tumor cells with the IOGC and removes them, while sparing healthy tissue. Commercially available low energy X- and gamma-ray emitting radioisotopes such as ^{201}Tl (69–83 keV), ^{99m}Tc (140 keV), and ^{123}I (156 keV) can be attached to the

---

* Corresponding author. Tel. +1 805 484 8300, fax +1 805 383 7185.

tumor seeking agent, and imaged using the IOGC HgI_2 array.

Motivation for this development comes from previous interest in non-imaging gamma- and beta-ray devices [1–11], and the need for the greater expected sensitivity and improved radiolabel localization with a small area imaging device. Furthermore, the superior energy resolution of HgI_2 detectors, compared with other room temperature detectors, can be utilized to enhance image contrast by the rejection of Compton scattered gamma-rays arising from the surrounding collimator and patient scatter environments.

2. Theoretical considerations on the choice of detector material

HgI_2 and CdTe are the most promising of the semiconductor gamma-ray detectors for configuration as arrays and for implementation in miniature probe applications. They do not need cryogenic cooling. They are superior to all scintillator and gas based systems due to their excellent signal-to-noise ratio. Excellent progress continues to be made in the improvement of both performance and availability of these materials [12,13].

Between the two semiconductor detectors, however, HgI_2 is favored. For detectors sufficiently thick to provide adequate efficiency over the interesting range of energies in nuclear medicine (80 to 200 keV), HgI_2 produces higher quality energy spectra. The overall shape of the spectra (Fig. 1), including low energy tailing (incomplete charge collection), appearance of anomalous peaks, etc. is generally much better for HgI_2 detectors [13,14]. Claims that CdTe is superior due to higher mobility-lifetime products are naive without consideration of the low electric fields that are practically obtained in these detectors and the resulting longer transit time for holes.

The superior quality of the HgI_2 energy spectra can be easily shown from theoretical considerations. In the clinical diagnostic energy range, the broadening of the photopeak linewidth and shift of counts from the photopeak to the low-energy tail and continuum is always dominated by trapping of charge carriers in the detector [14,15]. Generally, the major contributions determining the spectral response are due to electronic noise, statistical spreading of the photopeaks, and incomplete charge collection. Above 60 keV, spectroscopy is always dominated by degraded charge collection, due mostly to poor hole mobility and short hole trapping times relative to hole transit times, and is observed as the characteristic low energy spectral tailing (Fig. 1). In such trapping limited systems, a useful figure of merit is not simply the mobility-lifetime product but rather the ratio of hole transit time to trapping time, t_h/τ_h.

$$\frac{t_h}{\tau_h} = \frac{D}{v_{dh}\tau_h} = \frac{D}{(\mu_h\tau_h)E} = \frac{\ln(I_i/I_o)/\lambda}{(\mu_h\tau_h)E} = \frac{k}{(\mu_h\tau_h)E\lambda}, \quad (1)$$

where D is the detector thickness required to give detection efficiency I_i/I_o for a given gamma-ray energy, v_{dh} is the carrier drift velocity, μ_h is the hole mobility, E is the maximum electric field that the material will support with reasonable leakage currents, and λ is the linear attenuation coefficient for the particular detector material.

Smaller values of this metric (positive values less than one) correspond to more complete charge collection. Thus, the quality of the spectrum is inversely proportional to the product of μ_h, τ_h, E and λ. Even though $\mu_h\tau_h$ values for CdTe are slightly higher than for HgI_2 (using $\mu_h = 4 \text{ cm}^2 \text{ V}^{-1} \text{ s}^{-1}$ and $\tau_h = 10^{-5}$ s for HgI_2, and $\mu_h = 80 \text{ cm}^2 \text{ V}^{-1} \text{ s}^{-1}$ and $\tau_h = 10^{-6}$ s for CdTe), this is compensated by the much higher electric fields possible with HgI_2 (20 000 V/cm for HgI_2 and 1000 V/cm for CdTe). The limitations on electric field
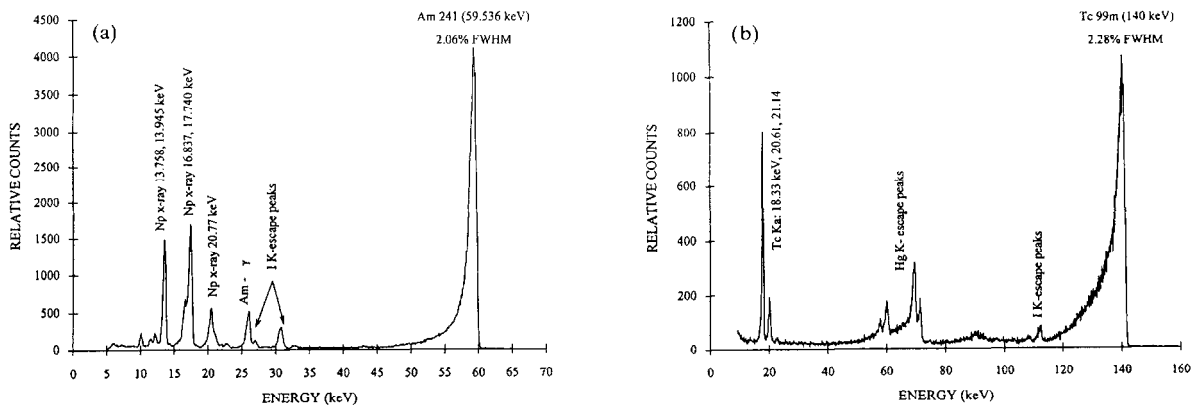

Fig. 1. Spectral measurement made with a 0.5 mm thick HgI_2 detector cooled to about 0°C with a Peltier cooler. Measurements made with (a) [241]Am source and (b) ^{99m}Tc source.

in CdTe detectors are associated with the lower resistivity of the material as well as the detector structures used [16]. Furthermore, the attenuation coefficients are much higher for HgI_2 (9.23 cm^{-1}) than CdTe (3.82 cm^{-1}) at 140 keV. These factors result in a superior metric for HgI_2 compared to CdTe by about one order of magnitude under optimal operating conditions for both detectors and by orders of magnitude for room temperature operation. Thus, in the clinical diagnostic energy range, the observed superior spectral performance of HgI_2 is explained by a consideration of all the pertinent parameters of these materials and their effect on charge collection.

3. Previous mercuric iodide imaging array design

Previously, 32 by 32 pixel HgI_2 arrays were fabricated and evaluated in a portable gamma camera configuration [18–20]. The square pixels had a nominal area of 1 mm by 1 mm, with 0.2 mm spacing between pixels. Detector thickness was typically 500 μm, which corresponds to about 37% stopping at 140 keV. The spatial resolution for ^{241}Am (59 keV), ^{133}Ba (356 keV), and ^{137}Cs (662 keV) was found to be 1.17 mm, 1.55 mm, and 1.93 mm full width at half maximum (FWHM), respectively. The spatial resolution was set by the electrode geometry up to about 200 keV (neglecting collimator effects), and therefore limited by the patterning technology. The energy resolution obtained at 59 keV was about 17.5% FWHM.

4. New detector array design

Several novel developments in the array design were implemented in the current work. Our goal was to greatly improve the state-of-the-art in HgI_2 array design. The specific objectives were to: (1) translate the detector design used to achieve the excellent single detector results (cf. Figs. 1a and 1b) to two-dimensional arrays, (2) design an array that minimizes inter-element crosstalk in the detector, (3) achieve thicker structures of at least 1.2 mm corresponding to about 67% stopping at 140 keV, (4) optimize the pixel geometry based on sensitivity (expected count rates under realistic clinical conditions) and spatial resolution requirements, and (5) characterize a prototype imaging device.

The detector design (Fig. 2) incorporated the advanced detector structure developed during optimization of single element X-ray detector structures and multi-element detector structures for EXAFS [21]. A novel discrete-pixel electrode patterning with adjacent

elements joined by thin wires [22] (as opposed to the typical parallel-line cross-grid array) incorporating guard rings was developed for the two-dimensional structure. With this approach, improved electric field distribution, hence improved charge collection, minimal crosstalk, and lower leakage currents were obtained compared with previous HgI_2 imaging array designs [18–20]. Fig. 3 shows a SILVACO simulation of the potential distribution in the inter-pixel region for the new discrete pixel patterning (A,B) versus that for the typical parallel-line cross grid array (C,D). The improved electrical definition of the pixels is evident.

HgI_2 crystals were evaluated and selected for array fabrication based upon both their electron and hole collection properties. Prototype arrays were fabricated on preselected crystalline slices by evaporation through physical masks. A detector is configured as a pseudo cross-grid array by connecting pixels to form "rows" on one side and "columns" on the other side of the device (Fig. 2). A novel hexagonal pixel geometry was designed to maximize the fill factor for the expected circular probe shape. Pixel dimensions are hexagonal with 1.5 mm or 1.9 mm diameters separated by 0.2 mm. The overall detector is a hexagon with a diameter of ~1 cm. The sensitive detector thickness is up to 1.2 mm, which corresponds to >99% efficiency at 59 keV and 67% efficiency at 140 keV. The HgI_2 detector is mounted on a ceramic substrate which is further mounted on a Teflon carrier that can be inserted into a socket in a test chamber in order to evaluate the array performance. Three prototype arrays were fabricated. All three arrays were operational. One of the devices with 1.9 mm pixels was then evaluated fully as described in the following sections.

Collimators with hexagonal holes matching the pixel geometries (1.5 mm or 1.9 mm "diameters") and septal wall thickness (0.2 mm) matching the inter-element spacings were fabricated from Nuclear Fields™ precision-cast high resolution nuclear medicine lead collimators. Each such collimator used with the IOGC prototypes was cut to a 1 cm length (height), and was adhered proximally to the detector surface.

Neglecting collimator effects, the spatial resolution of the imaging device is limited only by the pixel size, and very small pixels, approximately 250 μm, can be manufactured on HgI_2 using the standard evaporated contact technology. Too small a pixel size is unwarranted in this application, as the final image of a tumor bed would then be considerably count rate limited. Using patient data from a 2 cm^2 neck tumor with a 22 mCi bolus injection of ^{99m}Tc-sestamibi, the expected data rate was estimated to be ~100 counts per second (cps) before tumor removal. The pixel sizes for the prototype arrays were thus chosen to provide better resolution than standard scintillation imaging, but without unduly limiting the sensitivity.
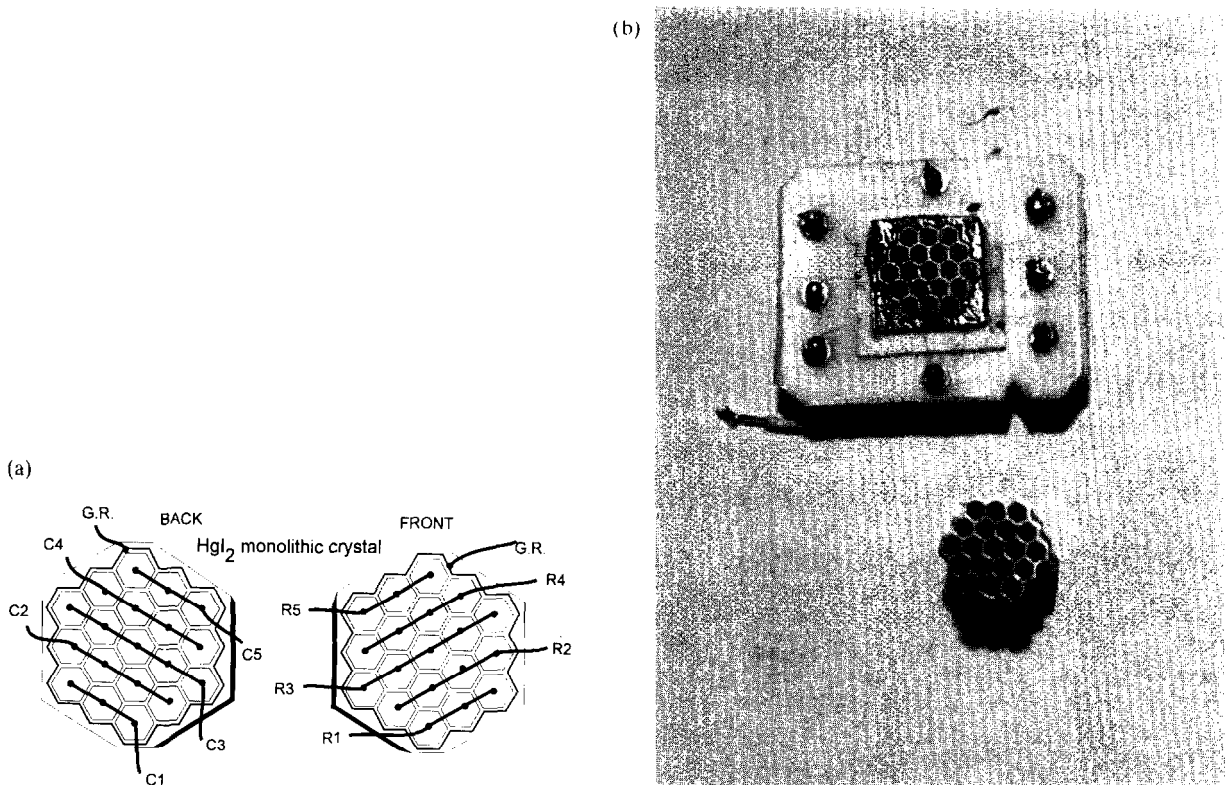
(b)

(a)

Fig. 2. (a) Schematic of electrode patterning with wire bonds on a monolithic HgI$_2$ crystal. The left image shows column electrodes on the lower surface; the right image shows orthogonal row electrodes on the proximal surface. (b) Photograph of the mounted detectors and the unattached collimator assembly.

5. Data acquisition and processing system

A test chamber with a thin beryllium window was developed for evaluating the prototype arrays. The chamber (left portion of Fig. 4) consists of a socket into which the detector arrays are inserted, followed by series of preamplifiers for the row and column signals. As in the standard cross-grid array architecture, a high voltage bias is applied across the detector (all row electrodes are at high voltage, and all column electrodes are at low voltage) producing an electric field density distribution maximized at the row/column intersections. When a gamma-ray is stopped in the detector, charge is produced which is then collected at the nearest row/column electrodes. The "pixels" are defined as the intersection of the row/column electrodes. Because the signals produced in both the row and column are due to the same electron and hole components, they are identical at the row and column electrodes except for polarity. In order to prevent floating the preamplifiers on the row (high voltage) side, they are decoupled (Fig. 4). Also, because the signals at the row and column electrodes are identical, the design was simplified by designating the directly coupled side of the detector as the "high-

resolution" side and further processing these signals using specially designed (Xsirius, Inc.) low noise preamplifier electronics. The decoupled side of the detector, which contains information concerning one axis of the spatial position of the signal but no new energy information, is processed by a commercial 8-channel hybrid preamplifier (LeCroy HQV 820).

The general philosophy of the post-processing was to simultaneously discretize all rows and columns upon the occurrence of a signal above a threshold (set just above the noise) in any of the column (high resolution) channels. Further processing and pixelation was then performed in software using coincidence logic. Four row and four column signals from the detector assembly, corresponding to fourteen pixels in the nineteen element assembly, fed NIM electronics for signal processing (Fig. 4). The four row (1st-axis spatial) signals were conditioned with "internal" low noise pre-amplifiers, and their output signals fed directly to shaping amplifiers (Ortec 855, 3 μs shaping). The four column (2nd-axis spatial and high spectral resolution) signals were fed to external pre-amplifiers (Ortec 113) in order to eliminate the DC offset. The column signals were then split into two branches: (1) amplifiers (3 μs shaping), and (2) linear
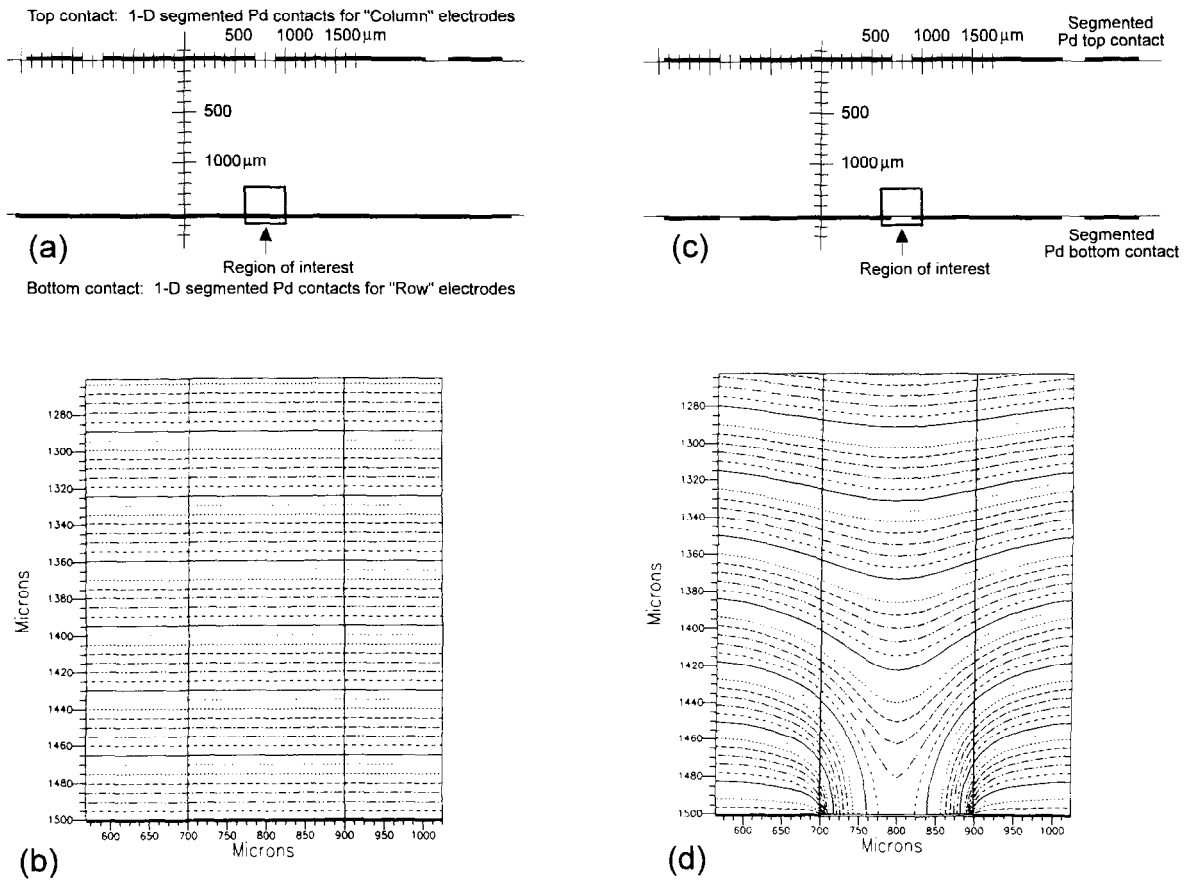
Fig. 3. 2-D SILVACO simulation of equipotential plots in the inter-pixel region for the new discrete pixel patterning (b) versus that for the typical parallel-line cross grid array (d). Physical structures of the discrete patterning and cross-grid-array patterning are shown in (a) and (c) respectively.

"or" (LeCroy 428F). The "or" column signals were then amplified (Tennelec TC203BLR, 4 µs shaping) and discriminated with a constant fraction timing SCA (Canberra 2035A). The timing SCA signal was delay adjusted with two gate and delay (Ortec 416A) modules in series. The tandem gates were used to minimize pile-up events, where the primary gate provided a long logic gate (2 µs) to a second, shorter gate (400 ns),
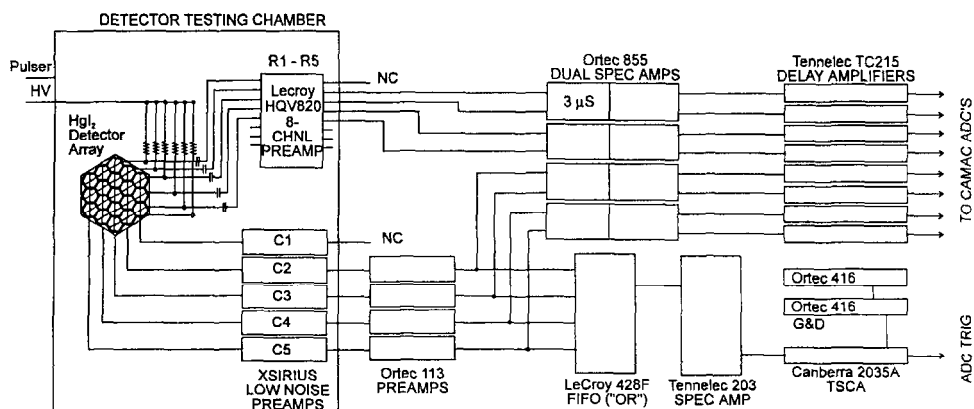

Fig. 4. Schematic of the electronics used for the multiplexed readout of the HgI$_2$ imaging array. The boxed area at the left was a specially constructed light tight Faraday chamber. Standard NIM electronics were used outside of box.

which provided the ADC trigger. All eight shaped and amplified row/column signals were delayed (Tennelec TC215) 4.57 μs to align the linear signals with the ADC trigger signal. The independent rows and columns were gain balanced prior to data collection. The signals were digitized with 12 bit fast ADCs (BiRa) driven via GPIB by LabVIEW™ software on a Macintosh IIfx platform. All data were collected in list mode for post processing on a VAX 4000 system.

The pixel data were histogrammed by first masking the four row and four column list mode data with user selectable energy windows, determined from the individual row and column spectra. Next, a coincidence was found between the rows and columns by selecting the intersection of coincidence of the highest digitized values of the rows and columns. Different energy windows could be independently selected for the rows and columns.

6. Energy resolution and flood field response measurements

The 1.9 mm pixel detector assembly was flood irradiated with ^{241}Am and ^{99m}Tc sources. Approximately 262k events were collected with a sealed 11 μCi ^{241}Am (59 keV), 1 mm diameter source, located 20 cm from the collimator assembly. In addition, approximately 655k events were collected with a 1 mCi ^{99m}Tc (140 keV), 0.7 mm diameter point source, located 50 cm from the collimator assembly.

The pixel spectral responses for ^{241}Am and ^{99m}Tc are shown in Figs. 5 and 6, respectively. The energy resolution for the photopeaks was calculated with various coincident energy windows (Fig. 7). Windows of the same width were used in the coincidence criterion for both rows and columns (decoupled and coupled sides). Note that the energy resolution im-
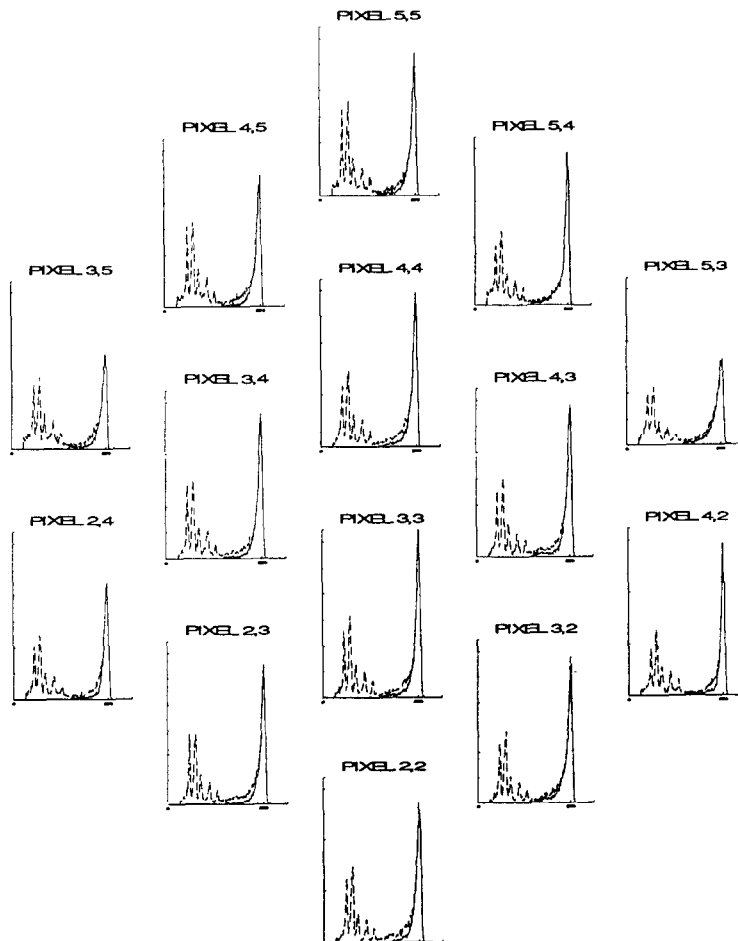

Fig. 5. Pixel spectral responses for the ^{241}Am source (column electrode). The figures show the same data set with 90% and 65% coincidence windows superimposed on the list mode data. Note that the integral photopeak counts (sensitivity) show little variation with coincidence energy windowing.
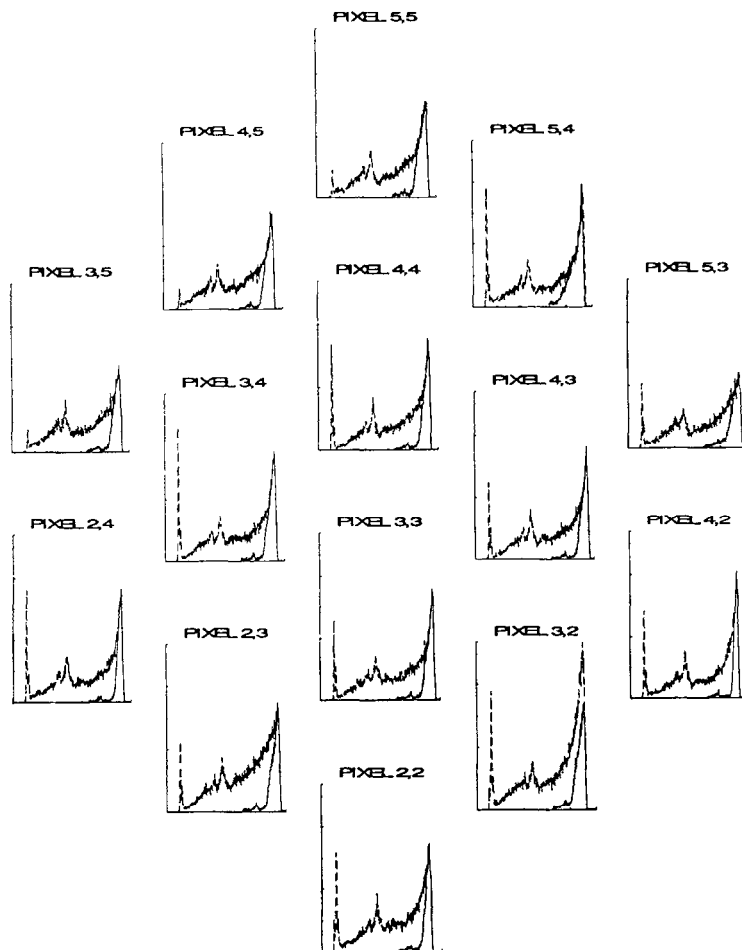
Fig. 6. Pixel spectral responses for the ^{99m}Tc source (column electrode). The figures show the same data set with 90% and 30% windows superimposed on the list mode data. Note that the integral photopeak counts (sensitivity) vary considerably with coincidence energy windowing, and that the energy resolution greatly improves with smaller window.
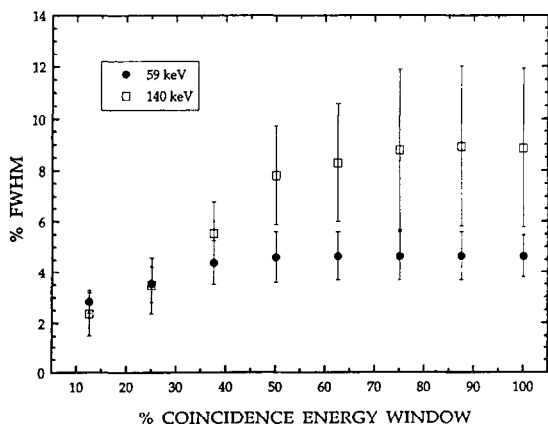

Fig. 7. Mean (column electrode) energy resolutions (% FWHM) for 14 pixels obtained for various coincident energy windows. Note the improved resolution with tighter coincident window constraints.

proves as the coincidence constraint is tightened. Multiple coincident events, comprised of more than one coincidence between rows and columns, were counted and discarded before further analysis. The number of multiples varied with the applied energy windows, and were always <2% of the total events recorded.

Note that the number of counts in the photopeak channel did not decrease substantially with the smaller coincident energy windows (superimposed plots in Figs. 5 and 6 are from the same data set, respectively). However, tightening the coincidence constraint did significantly reduce the low energy tailing as can be seen in the ^{99m}Tc (140 keV) spectra (Fig. 6). One explanation for this is that by applying a tighter coincidence constraint events with poorer hole collection were eliminated.

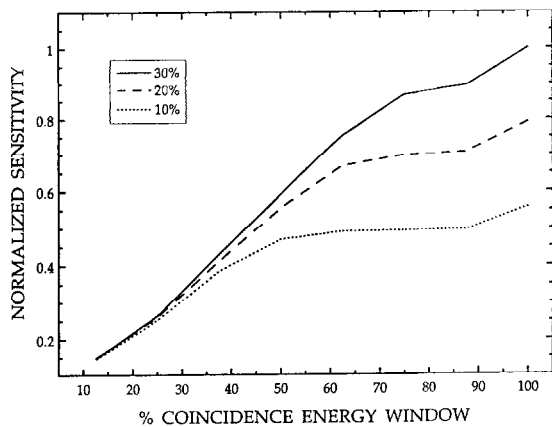The sensitivity was calculated with various co-

Fig. 8. Normalized (column electrode) sensitivity as a function of coincident energy windows measured as the integrated counts in three fixed ranges (10%, 20%, 30%) below the photopeak channel. Data is from the ^{99m}Tc (140 keV) flood irradiation.

incident energy windows (Fig. 8). The variation of the sensitivity (integrated counts) with coincidence criterion for three separate regions of integration: left edge

Table 1
Measured uniformity of the HgI$_2$ imaging array with low threshold of coincidence window set just above Compton edge of respective source photopeak energies

Source (energy)	Uniformity[a] ($\pm\sigma\%$) of integrated counts within given energy windows		
	10%	20%	30%
^{241}Am (59 keV)	12.1	11.0	11.3
^{99m}Tc (140 keV)	7.8	7.1	10.6

[a] Uniformity is defined as the variation in the counts per pixel over the entire imaging field of view.
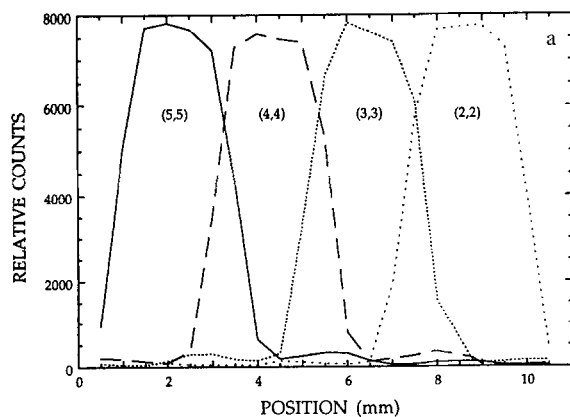
at 10%, 20%, and 30% below the photopeak are shown in Fig. 8.

The uniformity of the integrated counts collected in a window about the photopeak was measured for both ^{241}Am and ^{99m}Tc flood sources with the lower edge of the coincidence window placed just above the Compton edges of the sources. In the case of the ^{241}Am source, the lower edge of the row/column coincidence window was adjusted to about 15 keV whereas the Compton edge is 11.4 keV and in the case of the ^{99m}Tc source the lower edge of the window was at 52.5 keV which is slightly above the Compton edge at 49.6 keV. The choice of the coincidence window during the anticipated use of this technology will be determined by several factors including location of the Compton edge and the presence and location in the spectrum of scatter X-rays from the collimator. Thus for example if a lead collimator is used, the edge should be set above the Pb K-X rays. The observed uniformity variation for the flood field irradiation (Table 1) is attributed to misalignment of the collimator and detector and inherent non-uniformities in charge collection of the crystal.

The pixel gain uniformity was found to vary by only $\pm0.82\%$ for 59 keV and $\pm1.52\%$ for 140 keV. The discrete pixel spectral resolution, however, exhibited a larger variation (Fig. 7).

7. Pixel spatial response measurements

To characterize the spatial response of the array, the point sources were stepped in 0.5 mm increments along the face of the detector array. Several important features are illustrated in these spatial response measurements (Fig. 9 and Table 2).

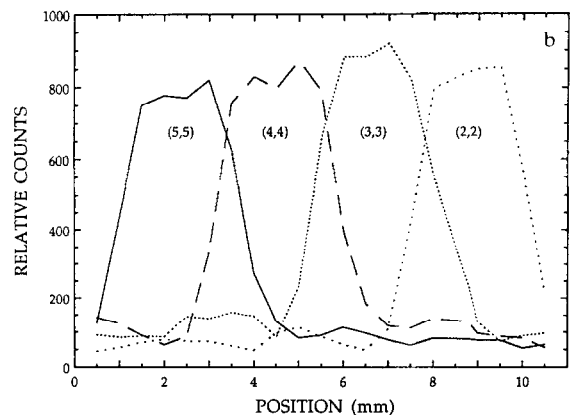One feature of Fig. 9 is the trapezoidal nature of the

Fig. 9. Spatial response of ^{241}Am (a) and ^{99m}Tc (b) point sources stepped in 0.5 mm increments along four pixels of the active fourteen element array. Note the trapezoidal nature of both data sets indicative of the pixel geometry. Note also the S/B difference between the sources. Numbers in parentheses under the curves designate the sampled pixel elements (row, column).

Table 2
Measured and theoretical spatial response of the 1.9 mm diameter pixel HgI$_2$ imagining array

	Source	
	[241]Am (59.6 keV)	[99m]Tc (140 keV)
Measured FWHM $\pm \sigma$ [mm]	2.71 ± 0.069	2.91 ± 0.099
Theoretical FWHM[a] [mm]	2.4 (2.89)	2.25 (2.59)
Measured FWTM $\pm \sigma$ [mm]	3.68 ± 0.17	4.42 ± 0.41
Theoretical FWTM[a] [mm]	2.8 (3.42)	2.59 (2.96)

[a] Values are for convolution of rectangular detector response with rectangular finite point source distribution. Paranthetic values for convolution of rectangular detector response and Gaussian point source distribution.

response function. The overall shape of the spatial response function is a convolution of the pixel geometry, the source shape, and the septal penetration function. The point spread function necessitates the deconvolution of these three factors. By simple geometric deconvolution of the data in Fig. 9. one can readily see that the point spread function does in fact approximate the pixel geometry (Fig. 9 and Table 2). There was <1% septal penetration contribution (calculated) at 59 keV and a maximum of 6.6% at 140 keV. Hence, the flat region across the face of any pixel indicates a relatively linear response within the septal boundaries of any one pixel.

The energy windows used to determine the pixel events were +25% / −40% (upper window/lower window) and +8.8% / −30% for the 59 keV and 140 keV photons, respectively. The low energy window was set just above the secondary peak closest to the photopeak in the spectrum, and the upper window was set substantially above the photopeak, in order to maximize the window. Due to the relatively narrow FWHM of the photopeaks, it was not necessary to investigate narrower energy windows. The "tuning" of the proper energy window does, however, affect the spatial resolution measurement.

The signal-to-background ($S/B \pm \sigma$, measured as the average max value/average min value) in the spatial response function measured 54.8 ± 3.4 and 9.20 ± 1.52 at 59 keV and 140 keV, respectively. The measured S/B values are therefore within a factor of 2 of the values predicted on the basis of the calculated septal penetration (i.e. S/B of 100 at 59 keV, and 15 at 140 keV). Deviation from these predicted values is likely due to non-zero ambient background.

The contrast ([max − min]/[max + min] $\pm \sigma$ where max and min are defined as before) was found to be 0.986 ± 0.016 and 0.799 ± 0.042 at 59 keV and 140 keV,

respectively. The contrast measure gives a better index of the ability to extract the true signal from the background, comprised of septal penetration and detector resolution effects.

8. Conclusions and future direction

Significant advancement has been made in the development of two dimensional HgI$_2$ detector array technology by incorporating previously developed principles for optimizing HgI$_2$ detector structures. Novel features of the detector structure include hexagonal pixel shapes and geometry designed to improve the electric fields and maximize the detector fill factor. Prototype 19 element HgI$_2$ intra-operative imaging devices with 1.5 mm and 1.9 mm pixels were successfully developed using these principles. A detector with sensitive thickness of 1.2 mm, corresponding to >99% efficiency at 59 keV and 67% efficiency at 140 keV was fabricated and evaluated. Pixel energy resolutions of 2.98% and 3.88% FWHM were obtained on the best individual pixels at 59 keV ([241]Am) and 140 keV (^{99m}Tc), respectively with a 30% coincidence window. Resolutions of 3.48% (59 keV) and 5.6% (140 keV) were obtained for these same pixels when the low edge of the coincidence window was set just above the Compton edge for each source.

The spatial resolution was found to be approximately equal to the geometric spacings of the electrode patterning (1.9 mm diameter pixels with 0.2 mm septal spacings). Ultimately, the pixel size of such a device could be made smaller, to achieve improved spatial resolution. The measured S/B was about 50% of what was predicted for gamma (septal) penetration of the 0.2 mm Pb collimator. The collimator effects on resolution have been well characterized for standard nuclear medicine gamma cameras and those principles obtain.

The effects of varying the energy windows on sensitivity and resolution were studied. In the current configuration, improved resolution was possible at the cost of sensitivity.

References

[1] H. Barber, J. Woolfenden, D. Donahue and W. Nevin, IEEE Trans. Nucl. Sci. NS-27 (1980) 496.

[2] D. Aitken, G. Hinkle, M. Thurston, S. Tuttle, D. Martin, J. Olsen, D. Haagensen, D. Houchens and E. Martin, Dis. Col. & Rect. 27 (1984) 279.

[3] J. Woolfenden, W. Nevin, H. Barber and D. Donahue, Chest 85 (1984) 84.

[4] D. Martin, G. Hinkle, S. Tuttle, J. Olsen, H. Nabi, D. Houchens, M. Thurston and E. Martin, Am. J. Surg. 150 (1985) 672.

[5] H. Reinhardt, D. Stura and O. Gratzl, Eur. Surg. Res. 17 (1985) 333.

[6] E. Martin, C. Mojsisik, G. Hinkle, J. Sampsel, M. Siddiqi, S. Tuttle, B. Sickle-Santanello, D. Colcher, M. Thurston, J. Bell, W. Farrar and J. Schlom, Am. J. Surg. 156 (1988) 386.

[7] H. Reinhardt, H. Meyer and E. Amrein, Eur. Surg. Res. 20 (1988) 51.

[8] H. Barber, H. Barret, J. Woolfenden, K. Myers and T. Hickernell, Phys. Med. Biol. 34 (1989) 727.

[9] C. Nieroda, C. Mojsisik, A. Sardi, P. Ferrara, G. Hinkle, M. Thurston and E. Martin, Dis. Col. & Rect. 32 (1989) 927.

[10] A. Sadr, M. Workman, C. Jojzisik, G. Hinkle, C. Nieroda and E. Martin, Arch. Surg. 124 (1989) 55.

[11] F. Daghighian, J.C. Mazziotta, E.H. Hoffman, P. Shenderov, B. Eshaghian, S. Siegel and M.E. Phelps, Med. Phys. 21 (1994) 153.

[12] For CdTe, see for example:
P. Siffert, Mat. Res. Soc. Proc. 16 (1983) 87;
G. Entine, P. Waer, T. Tiernan and M.R. Squillante, Nucl. Instr. and Meth. A 283 (1989) 282;
H. Tsutsui, T. Ohtsuchi, K. Ohmori and S. Baba, IEEE Trans. Nucl. Sci. NS-40 (1993) 40.

[13] For HgI$_2$, see for example:
A.J. Dobrowski, J.S. Iwanczyk, Y.J. Wang, J. Madden and J. Szawlowski, Proc. SPIE, 38th Symp. on Optical Instrumentation and Applied Engineering, Vol. 2007 (1993) 19.
J.S. Iwanczyk, MRS Symp. Proc. 302 (1993) 79;
V. Gerrish and L. van den Berg, Nucl. Instr. and Meth. A 299 (1990) 41.

[14] See for example, recent results in:
J.F. Butler, S.J. Friesenhahn, C. Lingren, B. Apotovsky, R. Simchon, F.P. Doty, W.L. Ashburn and W. Dillon, 1993 Nucl. Sci. Symp. & Med. Img. Conf. Rev. 1 (1993) 565;
J. Pantazis, A. Huber, P. Okun, M.R. Squillante, P. Waer and G. Entine, 1993 Nucl. Sci. Symp. & Med. Img. Conf. Rec. 1 (1993) 254.

[15] J.S. Iwanczyk, W.F. Schnepple and M.J. Masterson, Nucl. Instr. and Meth. A 322 (1992) 421.

[16] A.K. Khusainov, Nucl. Instr. and Meth. A 322 (1992) 335.

[17] J.S. Iwanczyk and B.E. Patt, Low noise electronics for X-ray and gamma-ray spectroscopy, in: Semiconductors for Room Temperature Nuclear Detector Applications, MRS Volume for Semiconductor Semimetals Series, eds. T.E. Schlesinger and R.B. James (Academic Press, 1995) in press.

[18] B.E. Patt, A. Del Duca, R. Dolin and C. Ortale, IEEE Trans. Nucl. Sci. NS-33 (1986) 523.

[19] B.E. Patt, A.G. Beyerle, R.C. Dolin and C. Ortale, Nucl. Instr. and Meth. A 283 (1989) 215.

[20] B.E. Patt, Mat. Res. Soc. Proc. 302 (1993) 43.

[21] J.S. Iwanczyk, N. Dorri, M. Want, R.W. Szezebiot, A.J. Dabrowski, B. Hedman, K. Hodgson and B.E. Patt, IEEE Trans. Nucl. Sci. NS-39 (1992) 1275.

[22] US Patent in preparation.